Ceramic Binder Jetting Additive Manufacturing: Effects of Particle Size on Feedstock Powder and Final Part Properties

Mohammadamin Moghadasi

Department of Engineering Technology and Industrial Distribution

Department of Materials Science and Engineering

Texas A&M University, TX 77843, USA

Ming Li

Department of Engineering Technology and Industrial Distribution

Department of Industrial and Systems Engineering, Texas A&M University, TX 77843, USA

Chao Ma*

Department of Engineering Technology and Industrial Distribution

Department of Materials Science and Engineering

Department of Industrial and Systems Engineering

Texas A&M University, TX 77843

Wenchao Du

Department of Industrial and Systems Engineering

Texas A&M University, TX 77843, USA

Zhijian Pei

Department of Industrial and Systems Engineering

Texas A&M University, TX 77843, USA

Keywords: Ceramics; Binder Jetting; Additive Manufacturing; Particle Size

* Corresponding author. E-mail address: cma@tamu.edu (Chao Ma)

Abstract

Binder jetting is a promising additive manufacturing method to fabricate a wide range of materials, including ceramics. The objective of this research is to investigate the effects of particle size on flowability and sinterability of the feedstock powder and resultant properties of fabricated parts. A commercial ceramic composite powder was sieved into three different particle size ranges: designated as fine, medium, and coarse powders, respectively. Flowability and sinterability measurements were performed on the sieved powders. After printing and sintering, the density of samples was measured with the Archimedes' method. Compressive tests were performed to investigate the mechanical properties of the fabricated parts. The experimental results showed that flowability increased, but sinterability decreased as particle size increased. The printed and sintered density was dependent on both flowability and sinterability: the highest density was achieved by the medium powder due to the balance between flowability and sinterability. The compressive strength was dominated by sinterability: the highest strength was achieved by the fine powder because of the highest sinterability.

1 Introduction

Due to the growing demand for durable materials in various applications [1,2], especially in severe conditions such as high temperature, extreme stress, corrosive environment, etc., the usage of ceramic materials is rapidly expanding in recent years [3]. Ceramic materials have many potential applications because of their outstanding properties such as high hardness, wear and heat resistance, as well as chemical inertness, and low density. In spite of the increasing need for ceramic materials, most conventional manufacturing processes are not capable of fabricating

complex-shaped ceramic parts at a reasonable cost. Actually, their high hardness, brittle nature, and negligible deformability make it very difficult, if not impossible, to fabricate complex-shaped parts using ceramic materials.

According to ASTM International (an international standards organization), additive manufacturing (AM) or 3D printing is defined as the process of joining materials layer by layer, which is different from the subtractive and formative manufacturing processes, to manufacture parts from 3D model data [4]. The main advantages of AM over conventional processes are the freedom of design, minimization of material consumption, reduction in the number of manufacturing operations, and cost-effective prototyping [5,6].

AM processes are divided into seven general categories [4]. Among the seven AM categories, binder jetting is a promising process to fabricate parts from a wide range of materials, especially ceramics [5,6]. The quality of the final part depends on parameters of feedstock powder (composition, particle size, particle morphology, etc.), binder (composition, concentration, wettability or reactivity with powder, etc.), printing (layer thickness, binder saturation, etc.), and post-processing (temperature, atmosphere, etc.). Therefore, a considerable amount of research has been focused on the aforementioned parameters to achieve desired part properties [5–14].

Recent research showed that the feedstock powder particle size had an impact on the quality of final parts in metal binder jetting [15–18]. Bai et al. [15] studied the effects of mixing copper powders of different particle sizes on properties of the powder and also printed and sintered parts. The flowability and packing density of the powder and the density of printed and sintered parts were improved by using the bimodal powder compared to the unimodal powder. However, the effects of particle size on properties of parts printed by unimodal powder were not the focus of the

study. Mostafei et al. [16] investigated the sintering behaviors of printed Inconel 625 samples with different particle size distributions. It was concluded that samples with a narrow particle size distribution (16-25 μm) showed a higher linear shrinkage, but samples with a wide particle size distribution (16-63 μm) demonstrated faster densification and also more pore elimination with high temperature sintering. Miyanaji et al. [17] studied the effects of particle size distribution of 316L stainless steel powder on the printed and sintered parts fabricated by binder jetting. Their results for three different-sized powders (with a median diameter of 14, 31, and 78 μm, respectively) showed that the density of printed and sintered parts was increased by decreasing the particle size of the powder.

However, ceramic powder could behave differently in binder jetting. The effect of particle size on ceramic binder jetting has not been much studied. Zocca et al. [14] compared lithium–aluminum–silicate glass–ceramic powders of two different sizes (75 and 223 μm) in binder jetting. The coarser powder showed better flowability (lower Hausner ratio), while the finer powder showed higher strut density and compressive strength. Both powders were relatively coarse. Effects of particle size might be different for a much finer powder.

The objective of the present study is to investigate the effects of the particle size on ceramic binder jetting in a wide range (0-150 μm) and relate the density and mechanical properties of printed and sintered parts to the feedstock powder characteristics such as flowability and sinterability.

2 Materials and Methods

2.1 Materials

In this work, a commercial ceramic composite powder (TP80 from MicroJet Technology Co.) was used as the raw material. Silica-based powder, like the TP80 powder, is known for the use in foundries and electrical industries as insulators. Table 1 shows the chemical composition (provided by the vendor) of the TP80 powder.

The TP80 ceramic powder was sieved into three particle size ranges, as listed in Table 2. According to the particle size ranges, the sieved powders are labeled as fine, medium, and coarse powders, respectively. Scanning electron microscopy (SEM) (Tescan Vega II) was used to examine the morphology of raw (unsieved) and sieved powders.

2.2 Printing and post-processing

Cylindrical samples with a diameter of 6 mm and a height of 10 mm were printed. Figure 1 schematically shows the printing process, which consists of four steps: lowering build plate, raising powder stock, spreading powder, and jetting binder. Firstly, the build plate is lowered by the defined height of a layer and the powder stock is raised by a height that is usually more than the defined height of a layer. Then the roller spreads the raised powder from the powder stock over the lowered build plate, forming a thin layer of loose powder. Thereafter, the print head selectively injects the binder according to the 3D model file and bond the loose powder in the defined areas. During the printing process, these aforementioned steps are repeated for each layer.

The binder jetting machine used for the fabrication of all samples was the ComeTrue® T10 3D printer manufactured by MicroJet Technology Co. All samples were printed with a water-based

clear binder (TB-31N) provided by MicroJet Technology Co., which was compatible with the TP80 powder and the T10 printer. The printing parameters are listed in Table 3.

The layer thickness is defined as the height of powder spread in each layer during the printing process. The print head of the T10 machine has four sets of nozzles for printing. The nozzle slot number determines which nozzle sets are employed to inject the binder during printing. Different nozzle set could be used to print colorful parts with different-colored binders. Vender is defined as the ratio of the amount of the powder provided by the powder stock, to the amount of the powder needed to fill a layer in the powder bed. This parameter allows the powder stock to provide extra powder for spreading, ensuring that the new layer is completely covered by the powder. Printing time sets the number of times that the nozzle injects the binder into each layer.

After printing, the whole job box, including green samples and loose powder, was placed in the oven at 35 °C for 2 h to cure the binder in the printed samples. The curing process served to provide the green samples with enough mechanical strength for removing the surrounding loose powder.

After curing, the samples were debound and sintered in a furnace (KSL-1700X-A1-UL from MTI Corp.). The debinding and sintering process profiles were provided by MicroJet Technology Co. These processes included several steps: heating up from room temperature to 500 °C, from 500 °C to 1150 °C, and from 1150 °C to 1250 °C with heating rates of 3.2 °C·min^{-1}, 2.4 °C·min^{-1}, and 0.8 °C·min^{-1}, respectively, and then dwelling at 1250°C for 30 min. Finally, the samples were cooled in the furnace to the room temperature.

2.3 Powder flowability measurement

Flowability of the powders were measured using two methods: repose angle and Hausner ratio [19,20]. In the repose angle method, the powder was let flow through a funnel into a cylindrical container until it overflowed and formed a cone-shaped powder pile on the top of the container. The repose angle was calculated from the measured height and radius of the formed powder cone. The measurements were repeated three times for each powder.

In the Hausner ratio method, the tap density and the apparent density of the powder were measured. To measure tap density, according to ASTM standard B213-17 [21], 100 g of powder was weighed and poured into a graduated cylinder. A tap density tester (DY-100A from DongGuan HongTuo Instrument Co.) was used to tap the graduated cylinder 3000 times with a stroke of 3 mm. The tap density was calculated by the weight of powder and the volume of the tapped powder in the graduated cylinder. The apparent density was measured by a Hall flowmeter funnel (DF-1-02 from DongGuan HongTuo Instrument Co.), based on ASTM standard B212-17 [22]. The powder was poured into the flowmeter funnel and ran through the flowmeter orifice into a cup with a volume of 25 cm^3. By measuring the weight of powder in the cup and knowing the volume of the cup, the apparent density was calculated. The Hausner ratio is equal to the ratio of the tap density to the apparent density.

2.4 Powder sinterability measurement

To investigate the effect of particle size on the sinterability of powders, three disc-shaped samples were prepared for each powder by cold pressing of 1 g of powder at a compressive stress of 100 MPa for 30 s in a cylindrical die with a diameter of 13 mm. The pressed discs were sintered based on the aforementioned heating profile. The bulk densities of the pressed and sintered samples

(i.e., the samples which were pressed and then sintered) were measured by the Archimedes' principle [23].

To study the effect of added binder on the thermal behavior of the printed sample, combined thermal gravimetric analysis (TGA) and differential scanning calorimetry (DSC) tests were conducted on the raw (unsieved) powder and the printed sample. The tests were conducted using a TA instruments Q-1000 analyzer, from room temperature to 1400°C with a heating rate of $10°C \cdot min^{-1}$.

2.5 Characterization of printed and sintered samples

In order to see the effect of the particle size on the quality of the printed and sintered samples (i.e., the samples which were printed and then sintered), the bulk density of the samples was measured by the Archimedes' principle [23]. The density measurements were conducted on three samples for each powder. The fracture surface of the printed and sintered samples was studied by SEM. The SEM images were taken on all fabricated samples to assess the microstructure. Compressive test was carried out on the printed and sintered samples by a universal testing machine (STM-100KN-E, United Testing Systems Inc., USA). According to ASTM standard [24], cylinders with a radius of 6.35 mm and a height of 12.7 mm were made with the binder jetting method. The strain rate of the compressive test was $0.2\ s^{-1}$ and the test was repeated at least four times for each type of sample.

3 Results and Discussion

3.1 Powder morphology

Figure 2 shows the SEM images of the raw (unsieved) powder. As can be seen from images, the powder particles are in the wide range of sizes, from less than 10 μm to larger than 150 μm. Moreover, the SEM images demonstrate that the particle shapes are not spherical. Figure 3 shows the SEM images of the powders sieved into different particle size ranges: fine (<53 μm), medium (53-90 μm), and coarse (90-150 μm). Small particles could be found in all of the three sieved powders probably because the sieving process could not completely filter all particles. Moreover, the sieved powders could agglomerate after sieving, and these agglomerates would look like large particles. However, the dominant particles became larger as the sieve size increased, indicating most particles were effectively separated by the sieving process.

3.2 Powder flowability

The repose angle and Hausner ratio are important indicators of powder flowability and quality of spreading process during the printing. Figure 4 shows the representative images taken during the repose angle test of the powders of different particle sizes. The measured repose angles are listed in Table 4. The repose angle of samples decreases as the powder particle size increases. Moreover, the Hausner ratio measurements are listed in Table 4. The Hausner ratio results agree with the repose angle results, as shown in Figure 5. The achieved results indicate that increasing the powder particle size decreases the Hausner ratio and repose angle of the powders and thus improves their flowability.

3.3 Powder sinterability

To compare the sinterability of the three powders of different particle sizes, the bulk density of the pressed and sintered samples is shown in Figure 6. By increasing the powder particle size, the density of pressed and sintered samples decreases. For the same amount of powder, the surface energy increases as the particle size decreases. Thus, higher sinterability and densification of the fine powder could be positively affected by the larger specific surface energy of the smaller particles.

To examine whether the sinterability measured on the feedstock powders was applicable to the printed green samples, the DSC-TGA results were compared between the raw powder and the printed sample. To cover all particle sizes in this study, raw (unsieved) powder was used for DSC-TGA testing, which included particles from less than 10 μm to larger than 150 μm, as shown in Figure 2. Figure 7(a) demonstrates the DSC-TGA results of the raw powder, including the weight change and heat flow. There is a large amount of weight loss from 40 °C to around 500 °C in the ceramic composite powder. This weight loss could be attributed to the different components in the ceramic composite. According to the previous research, the slight reduction in weight at approximately 100 °C was probably due to the evaporation of physically adsorbed water molecules on the silica [25,26]. Also, the potassium feldspar could show several weight losses and dehydration reactions from 140 °C to 350 °C because of various water molecule sites in the structure [27,28]. Moreover, Mothe et al. [29] reported a broad endothermic peak in the range of 500 to 600 °C, depending on the heating rate, because of the dehydroxylation of the kaolinite.

The DSC-TGA results of the printed sample are shown in Figure 7(b). The comparison between the raw powder and the printed sample could show the influence of added binder on the

thermal behavior. The elimination of some peaks in the DSC plot and decline in the total amount of weight loss in the TGA plot of printed samples could be related to the curing process performed on the printed sample. As mentioned before, the curing process was performed to slightly strengthen the printed samples to avoid breaking them during removing the loose powder. Therefore, some reactions, such as evaporation of water or dehydration, might be partially done during the curing process. However, in the high temperature range (>600 °C), the TGA and DSC plots of the raw powder and printed sample look similar, indicating the presence of added binder in the printed sample has a negligible influence on the sintering process (>600 °C). Therefore, it was concluded that sinterability measured on the feedstock powders was applicable to printed samples.

3.4 Printed and sintered density

As previously discussed, the sinterability of feedstock powders with different particle sizes was studied by pressing and sintering the powders (Figure 6), without including the binder jetting process. To investigate the effect of particle size on the binder jetting process, the bulk densities of the printed and sintered samples were measured. Figure 8 shows the bulk densities of printed and sintered samples. As it is shown, the bulk density is slightly increased for the medium (53-90 μm) powder samples in comparison with the fine (<53 μm) powder samples, and then decreased for the coarse (90-150 μm) powder samples. This trend of increase and then decrease in the density of printed and sintered samples with different particle sizes could be related to the properties of the feedstock powders.

To investigate the relation between the density of printed and sintered samples and the properties of the powder, the printed and sintered density, the flowability (repose angle selected as

the metric), and the sinterability results are consolidated and shown in Figure 9. By increasing the particle sizes, the flowability of powder increases (the repose angle decreases) while the sinterability decreases (the pressed and sintered density decreases). These two competing mechanisms govern the final printed and sintered density. Compared to the fine (<53 μm) powder samples, the improvement in the bulk density of the medium (53-90 μm) powder samples could be related to the increase in the flowability of the medium (53-90 μm) powder, and as a result, the improvement in the powder spreading step during the printing process. But by increasing the particle size from the medium powder to the coarse powder, even though the flowability is further enhanced, the bulk density of the coarse powder is decreased compared to the medium powder samples. The reduction in the bulk density of the coarse powder samples could be attributed to the decrease in sinterability due to the existence of large particles and thus the formation of large pores in the structure of the coarse powder samples. Therefore, although the flowability of the coarse powder is improved, the relative density is declined in comparison to the fine and medium powder samples.

3.5 Microstructure of printed and sintered samples

Figure 10 shows the microstructure of the printed and sintered samples. The images were taken by SEM from the fracture surfaces of fabricated samples with different particle sizes. The microstructure of the coarse (90-150 μm) powder sample shows the formation of large pores which were distributed uniformly in all parts of the structure. Although the powder was uniformly distributed in the powder bed after spreading because of the appropriate flowability of the coarse powder, a significant fraction of pores could be seen in the SEM images due to the low sinterability

of the coarse powder and thus the formation of large pores. The formation of these large pores in the coarse powder samples leads to the low density.

On the contrary, as could be seen in the SEM image of the fine (<53 μm) powder sample, the pores were not uniformly distributed in the structure of the printed and sintered sample. In spite of the high sinterability of the fine powder and the proper bonding between the small particles, the large and continuous pores were formed due to the improper flowability of the powder. Some large pores are shown by the yellow arrows in Figure 10. Since the fine powder has a low flowability, the build plate could not be entirely covered by powder during spreading and therefore large and continuous pores were formed in the structure due to the lack of powder in the layer.

In the case of the medium (53-90 μm) powder, because of the better flowability compared to the fine powder and better sinterability compared to the coarse powder, the lowest pore fraction was achieved.

3.6 Mechanical properties of printed and sintered samples

The results of compressive tests performed on the printed and sintered samples with different particle sizes are plotted in Figure 11. Regardless of the particle size, it can be concluded that the strength of all printed and sintered samples is quite low. It is attributed to the low density of the printed and sintered samples. Furthermore, comparing the compression results across different particle sizes, it shows that by increasing the particle size, the strength of printed and sintered samples decreases. The decrease in the strength might be related to low sinterability and thus the formation of the large pores between the large particles in the medium (53-90 μm) and the coarse (90-150 μm) powder samples.

4 Conclusions

The effects of the feedstock powder particle size on the properties of the powder as well as the printed and sintered samples from the binder jetting additive manufacturing process were studied experimentally. Increasing the particle size improved the flowability but decreased the sinterability of the powder. By increasing the powder particle size, the density of printed and sintered samples was slightly increased due to the improvement in the powder flowability and then significantly decreased because of the decline in the powder sinterability. The strength of the printed and sintered samples was increased by decreasing the powder particle size. The high sinterability of the fine powder could be the main reason for its highest mechanical strength.

Acknowledgements

This material is based upon work supported by the National Science Foundation under Grant No. 1762341.

References

[1] N.P. Padture, Advanced structural ceramics in aerospace propulsion, Nat. Mater. 15 (2016) 804–809. doi:10.1038/nmat4687.

[2] M.A. Moghadasi, M. Nili-Ahmadabadi, F. Forghani, H.S. Kim, Development of an oxide-dispersion-strengthened steel by introducing oxygen carrier compound into the melt aided by a general thermodynamic model, Sci. Rep. 6 (2016) 1–10. doi:10.1038/srep38621.

[3] E.C. Hammel, O.L.-R. Ighodaro, O.I. Okoli, Processing and properties of advanced porous ceramics: An application based review, Ceram. Int. 40 (2014) 15351–15370.

doi:10.1016/j.ceramint.2014.06.095.

[4] Standard Terminology for Additive Manufacturing – General Principles – Terminology, ASTM Int. (2015) 1–9. doi: 10.1520/ISOASTM52900-15.

[5] X. Lv, F. Ye, L. Cheng, S. Fan, Y. Liu, Binder jetting of ceramics: Powders, binders, printing parameters, equipment, and post-treatment, Ceram. Int. 45 (2019) 12609–12624. doi:10.1016/j.ceramint.2019.04.012.

[6] W. Du, X. Ren, C. Ma, Z. Pei, Binder Jetting Additive Manufacturing of Ceramics: A Literature Review, ASME 2017 Int. Mech. Eng. Congr. Expo., (2017) doi:10.1115/IMECE2017-70344.

[7] W. Du, X. Ren, C. Ma, Z. Pei, Ceramic binder jetting additive manufacturing: Particle coating for increasing powder sinterability and part strength, Mater. Lett. 234 (2019) 327–330. doi:10.1016/j.matlet.2018.09.118.

[8] W. Du, G. Miao, L. Liu, Z. Pei, C. Ma, Binder jetting additive manufacturing of ceramics: Comparison of flowability and sinterability between raw and granulated powders, ASME 2019 14th Int. Manuf. Sci. Eng. Conf., (2019) doi:10.1115/MSEC2019-2983.

[9] G. Miao, W. Du, Z. Pei, C. Ma, Binder jetting additive manufacturing of ceramics: Analytical and numerical models for powder spreading process, ASME 2019 14th Int. Manuf. Sci. Eng. Conf., (2019) doi:10.1115/MSEC2019-2925.

[10] W. Du, X. Ren, Y. Chen, C. Ma, M. Radovic, Z. Pei, Model Guided Mixing of Ceramic Powders With Graded Particle Sizes in Binder Jetting Additive Manufacturing, ASME 2018 13th Int. Manuf. Sci. Eng. Conf., (2018) doi:10.1115/MSEC2018-6651.

[11] H. Miyanaji, S. Zhang, A. Lassell, A. Zandinejad, L. Yang, Process Development of Porcelain Ceramic Material with Binder Jetting Process for Dental Applications, Miner. Met. Mater. Soc. 68 (2016) 831–841. doi:10.1007/s11837-015-1771-3.

[12] P. Nandwana, A.M. Elliott, D. Siddel, A. Merriman, W.H. Peter, S.S. Babu, Powder bed binder jet 3D printing of Inconel 718: Densification, microstructural evolution and challenges☆, Curr. Opin. Solid State Mater. Sci. 21 (2017) 207–218. doi:10.1016/j.cossms.2016.12.002.

[13] S.M. Gaytan, M.A. Cadena, H. Karim, D. Delfin, Y. Lin, D. Espalin, E. MacDonald, R.B. Wicker, Fabrication of barium titanate by binder jetting additive manufacturing technology, Ceram. Int. 41 (2015) 6610–6619. doi:10.1016/j.ceramint.2015.01.108.

[14] A. Zocca, C.M. Gomes, E. Bernardo, R. Müller, J. Günster, P. Colombo, LAS glass-ceramic scaffolds by three-dimensional printing, J. Eur. Ceram. Soc. 33 (2013) 1525–1533. doi:10.1016/j.jeurceramsoc.2012.12.012.

[15] Y. Bai, G. Wagner, C.B. Williams, Effect of particle size distribution on powder packing and sintering in binder jetting additive manufacturing of metals, J. Manuf. Sci. Eng. 139 (2017) 1–6. doi:10.1115/1.4036640.

[16] A. Mostafaei, P. Rodriguez De Vecchis, I. Nettleship, M. Chmielus, Effect of powder size distribution on densification and microstructural evolution of binder-jet 3D-printed alloy 625, Mater. Des. 162 (2019) 375–383. doi:10.1016/j.matdes.2018.11.051.

[17] H. Miyanaji, N. Momenzadeh, L. Yang, Effect of powder characteristics on parts fabricated via binder jetting process, Rapid Prototyp. J. 25 (2019) 332–342. doi:10.1108/RPJ-03-2018-

0069.

[18] M. Li, W. Du, A. Elwany, Z. Pei, C. Ma, Binder jetting additive manufacturing of metals: A literature review, ASME 2019 14th Int. Manuf. Sci. Eng. Conf., (2017) doi:10.1115/MSEC2019-2994.

[19] Standard Test Method for Measuring the Angle of Repose of Free-Flowing Mold Powders, ASTM Int. (2000) 15–16. doi:10.1520/C1444-00.

[20] R.O. Grey, J.K. Beddow, On the Hausner Ratio and its relationship to some properties of metal powders, Powder Technol. 2 (1969) 323–326. doi:10.1016/0032-5910(69)80024-0.

[21] Standard Test Method for Tap Density of Metal Powders and Compounds, ASTM Int. (2015) 15–18. doi:10.1520/B0527-15.

[22] Standard Test Method for Apparent Density of Free-Flowing Metal Powders Using the Hall Flowmeter Funnel, ASTM Int. 2 (2017) 89–91. doi:10.1520/B0212-17.

[23] Standard Test Methods for Density of Compacted or Sintered Powder Metallurgy (PM) Products Using Archimedes' Principle, ASTM Int. (2013) 1–7. doi:10.1520/B0962-17.

[24] Standard Test Method for Monotonic Compressive Strength of Advanced Ceramics at Ambient Temperature, ASTM Int. 10 (2015) 1–13. doi:10.1520/C1424-10.

[25] J.W. Cho, K. Sul, Characterization and properties of hybrid composites prepared from poly(vinylidene fluoride–tetrafluoroethylene) and SiO_2, Polymer. 42 (2001) 727–736. doi:10.1016/s0032-3861(00)00371-2.

[26] R.K. Nagarale, G.S. Gohil, V.K. Shahi, R. Rangarajan, Organic−Inorganic Hybrid

Membrane: Thermally Stable Cation-Exchange Membrane Prepared by the Sol−Gel Method, Macromolecules. 37 (2004) 10023–10030. doi:10.1021/ma048404p.

[27] P. Ballirano, G. Cametti, Dehydration dynamics and thermal stability of erionite-K: Experimental evidence of the “internal ionic exchange” mechanism, Microporous Mesoporous Mater. 163 (2012) 160–168. doi:10.1016/j.micromeso.2012.06.059.

[28] A. Bloise, M. Catalano, E. Barrese, A.F. Gualtieri, N.B. Gandolfi, S. Capella, E. Belluso, TG/DSC study of the thermal behaviour of hazardous mineral fibres, J. Therm. Anal. Calorim. 123 (2016) 2225–2239. doi:10.1007/s10973-015-4939-8.

[29] C.G. Mothé, M.C.R. Ambrósio, Processes occurring during the sintering of porous ceramic materials by TG/DSC, J. Therm. Anal. Calorim. 87 (2007) 819–822. doi:10.1007/s10973-006-8196-8.

Tables and Figures

Table 1. The chemical composition of the TP80 ceramic composite powder

Component	*Crystalline silica (quartz)*	*Kaolinite*	*Potassium feldspar*
Fraction (wt.%)	50	25	25

Table 2. The particle size ranges of the TP80 powder used for the experiment

Designation	*Fine*	*Medium*	*Coarse*
Particle size ranges	< 53 μm	53 μm < - < 90 μm	90 m < - < 150 μm

Table 3. The printing parameters used

Printing parameter	*Value*
Layer thickness (mm)	0.16
Nozzle slot number	2
Vender	1.4
Printing time	1

Table 4. Flowability results of different powders

Powder	*Fine*	*Medium*	*Coarse*
Particle size ranges	*< 53 μm*	*53 μm < - < 90 μm*	*90 μm < - < 150 μm*
Repose angle	*52.1 ± 1.6*	*41.9 ± 1.8*	*33.6 ± 0.5*
Apparent density (g/cm^3)	*0.4*	*0.8*	*0.7*
Tap density (g/cm^3)	*1.1*	*1.1*	*0.8*
Hausner ratio	*2.6*	*1.4*	*1.3*

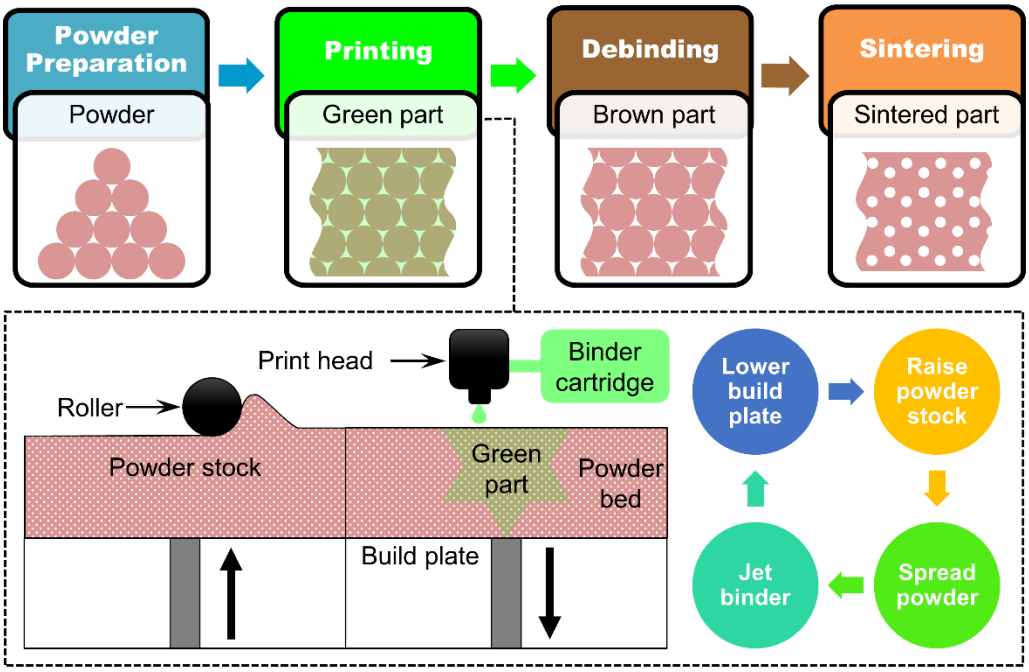

Figure 1. Steps of binder jetting additive manufacturing

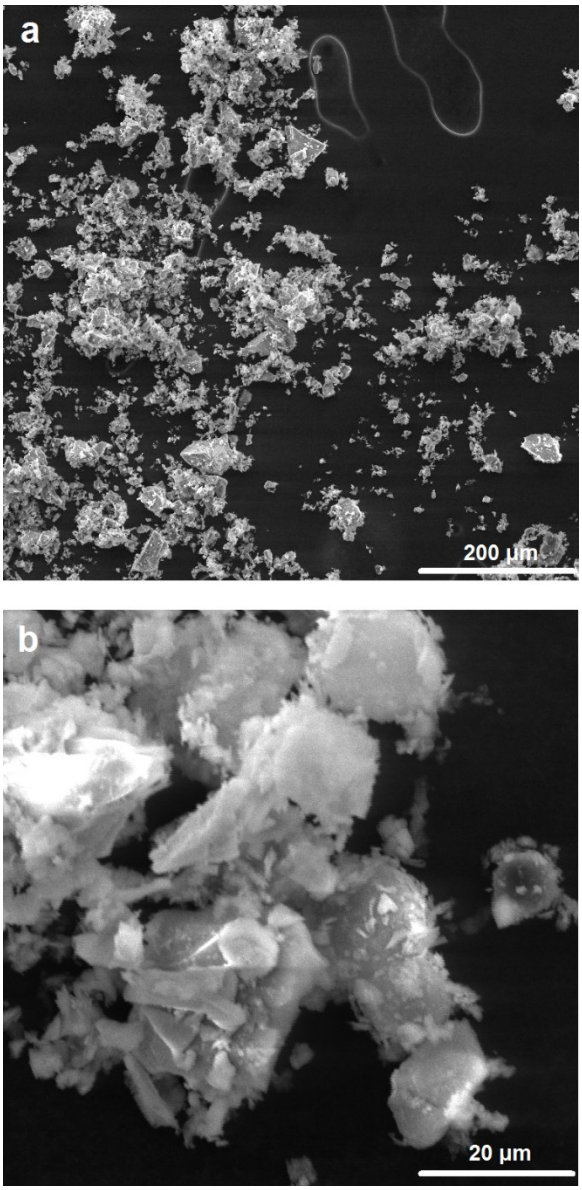

Figure 2. SEM images of the raw (unsieved) powder

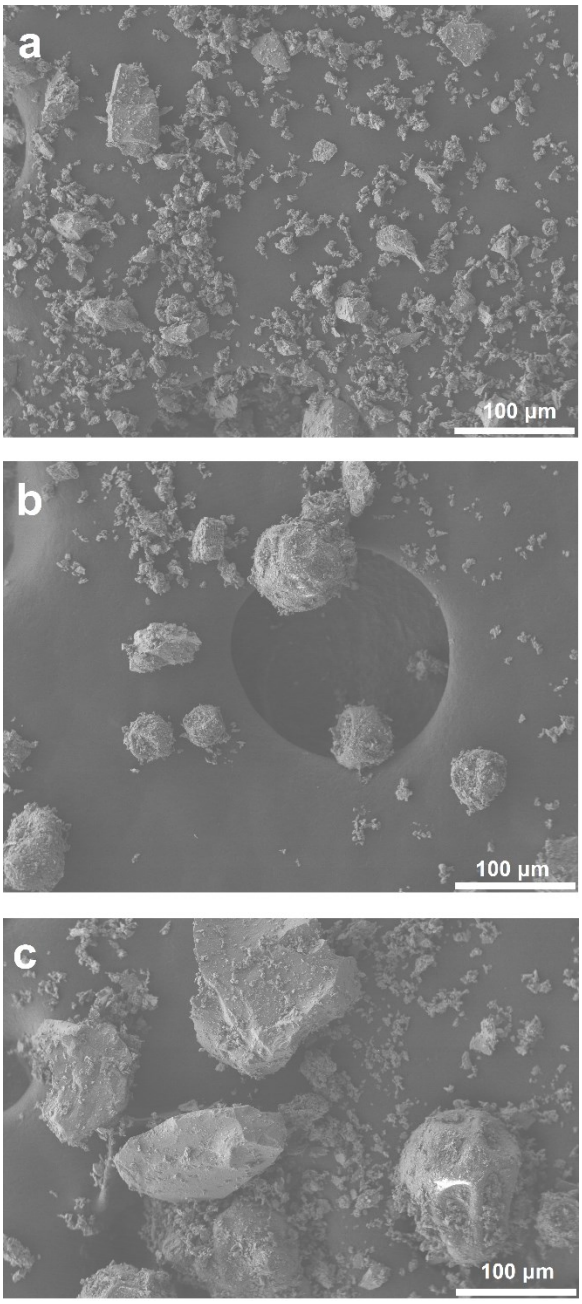

Figure 3. SEM images of the sieved powders of different particle sizes: a) fine (<53 µm), b) medium (53-90 µm), and c) coarse (90-150 µm)

Figure 4. Images of the repose angles of the sieved powders of different particle sizes: a) fine (<53 μm), b) medium (53-90 μm), and c) coarse (90-150 μm)

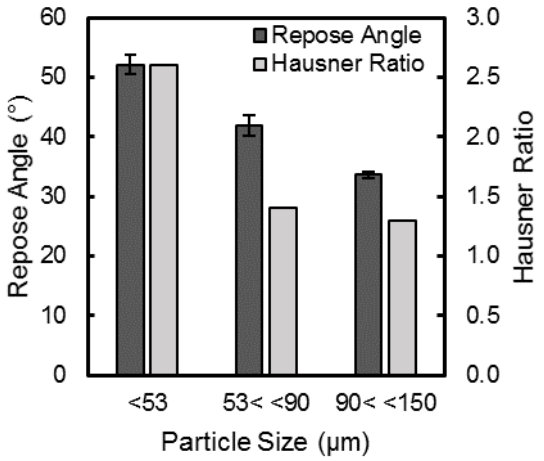

Figure 5. Flowability (repose angle and Hausner ratio) of the sieved powders of different particle sizes

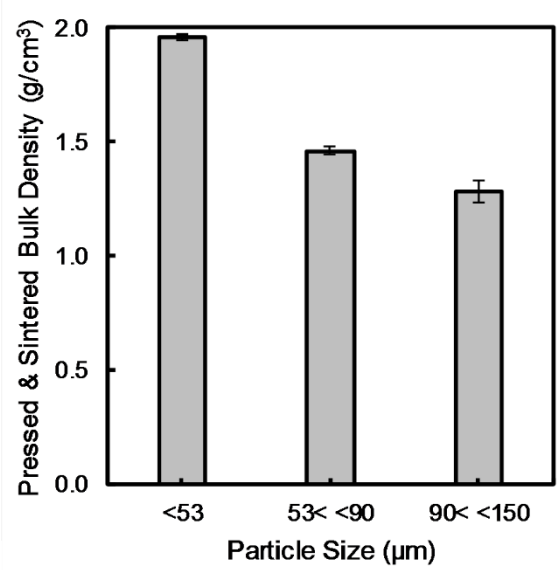

Figure 6. Sinterability (bulk density of pressed and sintered samples) of the sieved powders of different particle sizes

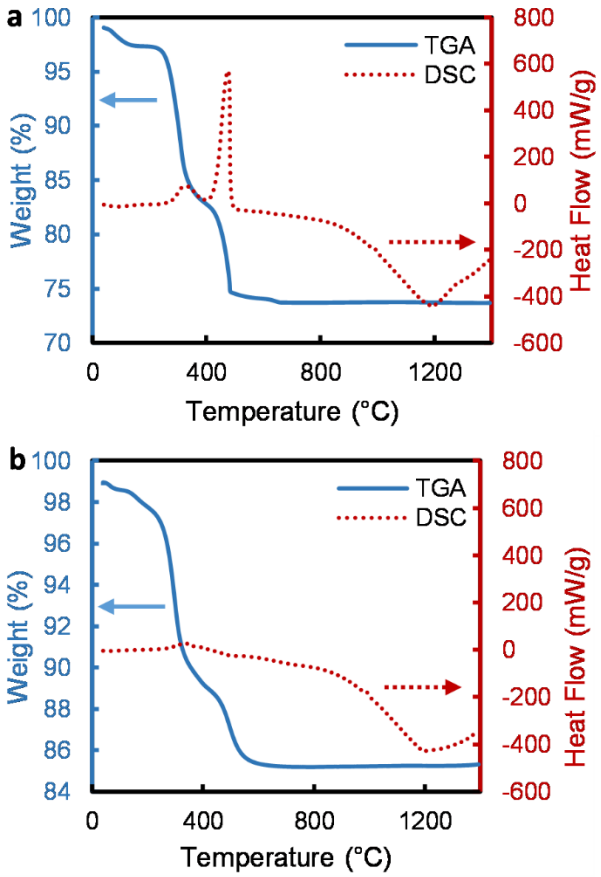

Figure 7. TGA-DSC results of the a) raw (unsieved) powder and b) printed sample

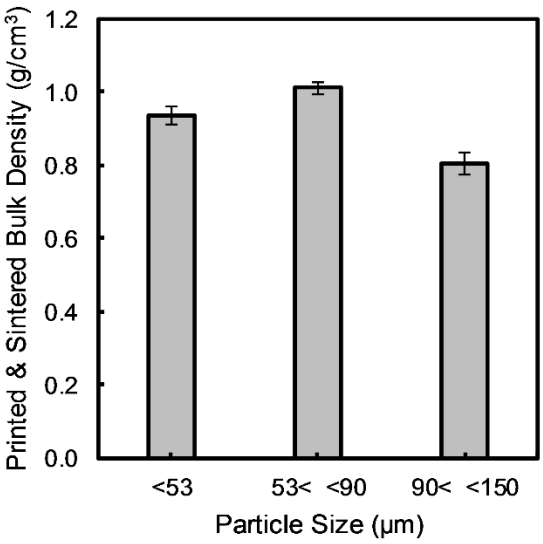

Figure 8. The bulk density of printed and sintered samples from the sieved powders of different particle sizes

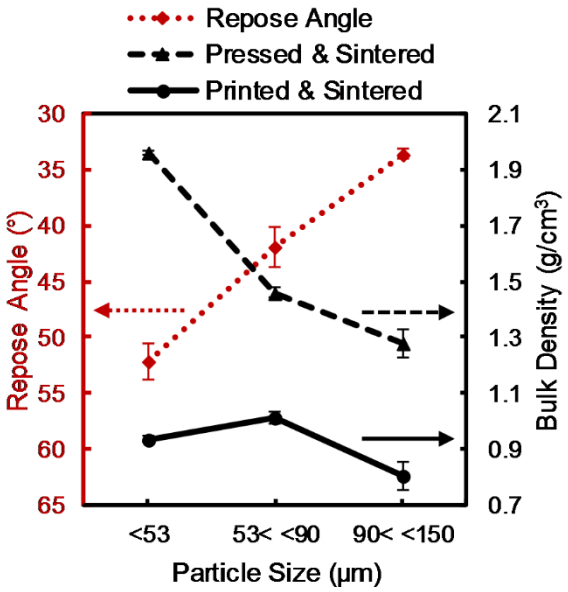

Figure 9. The flowability (repose angle) and sinterability (pressed and sintered bulk density) of the sieved powders of different particle sizes and their resultant printed and sintered bulk density

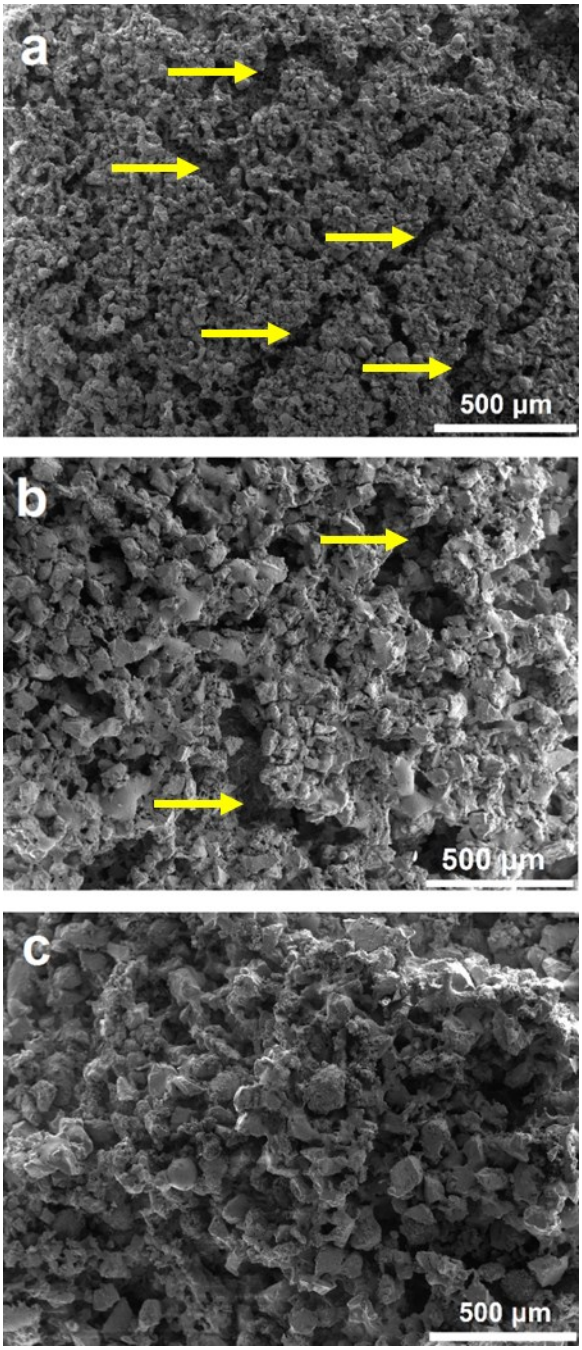

Figure 10. SEM images of the fracture surfaces of printed and sintered samples from the sieved powders of different particle sizes: a) fine (<53 µm), b) medium (53-90 µm), and c) coarse (90-150 µm) powders (yellow arrows show the pores in the structure of samples)

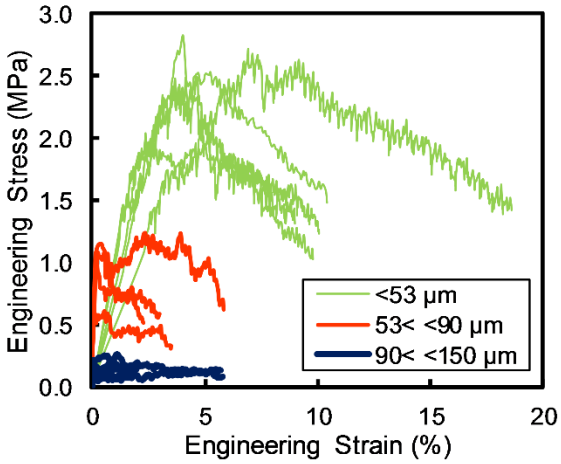

Figure 11. Stress-strain curves from compressive tests on the printed and sintered samples from the sieved powders of different particle sizes